Inorganic Chemistry

pubs.acs.org/IC Article

$Tl_2Ir_2O_7$: A Pauli Paramagnetic Metal, Proximal to a Metal Insulator Transition

Hai L. Feng, Chang-Jong Kang, Zheng Deng, Mark Croft, Sizhan Liu, Trevor A. Tyson, Saul H. Lapidus, Corey E. Frank, Youguo Shi, Changqing Jin, David Walker, Gabriel Kotliar, and Martha Greenblatt*

Cite This: *Inorg. Chem.* 2021, 60, 4424−4433 Read Online

ACCESS | Metrics & More | Article Recommendations

ABSTRACT: A polycrystalline sample of $Tl_2Ir_2O_7$ was synthesized by high-pressure and high-temperature methods. $Tl_2Ir_2O_7$ crystallizes in the cubic pyrochlore structure with space group $Fd\bar{3}m$ (No. 227). The Ir^{4+} oxidation state is confirmed by Ir−L_3 X-ray absorption near-edge spectroscopy. Combined temperature-dependent magnetic susceptibility, resistivity, specific heat, and DFT+DMFT calculation data show that $Tl_2Ir_2O_7$ is a Pauli paramagnetic metal, but it is close to a metal−insulator transition. The effective ionic size of Tl^{3+} is much smaller than that of Pr^{3+} in metallic $Pr_2Ir_2O_7$; hence, $Tl_2Ir_2O_7$ would be expected to be insulating according to the established phase diagram of the pyrochlore iridate compounds, $A^{3+}{}_2Ir^{4+}{}_2O_7$. Our experimental and theoretical studies indicate that $Tl_2Ir_2O_7$ is uniquely different from the current $A^{3+}{}_2Ir^{4+}{}_2O_7$ phase diagram. This uniqueness is attributed primarily to the electronic configuration difference between Tl^{3+} and rare-earth ions, which plays a substantial role in determining the Ir−O−Ir bond angle, and the corresponding electrical and magnetic properties.

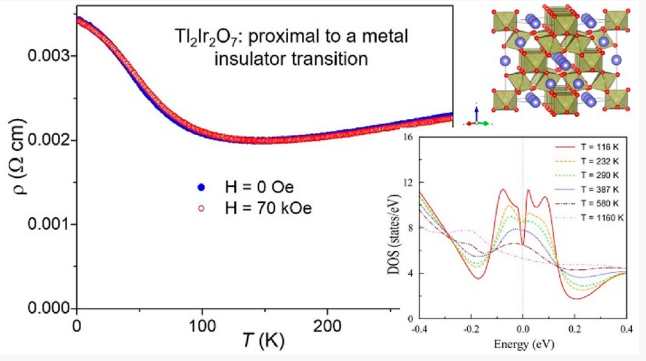

INTRODUCTION

The 5d oxides are attracting intensive studies owing to their fascinating physical properties, such as a Mott insulating state driven by spin−orbit coupling (SOC) in Sr_2IrO_4,[1] a ferroelectric metal $LiOsO_3$,[2] metal−insulator transition (MIT),[3] superconductor,[4] and high-temperature ferromagnetic or ferrimagnetic insulator/half-metal materials.[5−8] Compared to 3d electrons, 5d electrons present much stronger SOC, weaker Coulomb interactions, and thus provide a unique platform to study correlated electronic systems.[9]

The iridium pyrochlores, $A^{3+}{}_2Ir^{4+}{}_2O_7$ (A = Bi, Y, or a lanthanide ion), display a fascinating phase diagram.[10−31] Studies of these iridium pyrochlores indicate that the physical properties are generally correlated to the ionic size of A^{3+} ions, which determine the trigonal distortions of IrO_6 octahedra and Ir−O−Ir bond angles, thereby affecting the hopping between Ir electrons.[9,32] $Bi_2Ir_2O_7$ and $Pr_2Ir_2O_7$ with relatively large A^{3+} cations are metallic,[10,16,19,25] while others with smaller A^{3+} ions are antiferromagnetically ordered and electrically insulating at low temperatures;[17,18,21,27,31] particularly, Nd_2Ir_2O7, $Sm_2Ir_2O_7$, and $Eu_2Ir_2O_7$ show MIT.[12,21,28−30]

Here, we report the synthesis, crystal structure, and magnetic and electrical properties of a new iridate pyrochlore, $Tl_2Ir_2O_7$. The Shannon effective ionic radius of Tl^{3+} (0.98 Å) is comparable to those of Yb^{3+} (0.985 Å) and Lu^{3+} (0.977 Å), and an insulating state is expected for $Tl_2Ir_2O_7$, as both $Yb_2Ir_2O_7$ and $Lu_2Ir_2O_7$ are insulating. However, our studies find that $Tl_2Ir_2O_7$ is a Pauli paramagnetic metal and is close to a MIT.[33]

EXPERIMENTAL SECTION

Sample Preparation. Powders of Tl_2O_3 (Alfa, 99.9%) and IrO_2 (Alfa, 99.99%) with a molar ratio of 1:2 were weighed and mixed well using a mortar and pestle. The IrO2 was heated overnight at 1173 K before using. The powders were then sealed in a Pt capsule, which was placed inside a MgO crucible. They were statically compressed at a pressure of 5 GPa in a Walker-type multianvil press and heated at 1373 K for 2 h before quenching to ambient pressure while keeping the pressure stable. Then the pressure was released gradually.

Synchrotron Powder X-ray Diffraction (SPXD). Part of the $Tl_2Ir_2O_7$ sample was ground to a fine powder, which was then characterized by SPXD (λ = 0.41273 Å) at ambient temperature at Beamline 11-BM of the Advanced Photon Source (APS) of Argonne National Laboratory. Rietveld refinements of the powder diffraction

Received: October 21, 2020
Published: March 11, 2021

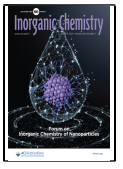

https://dx.doi.org/10.1021/acs.inorgchem.0c03124
Inorg. Chem. 2021, 60, 4424−4433

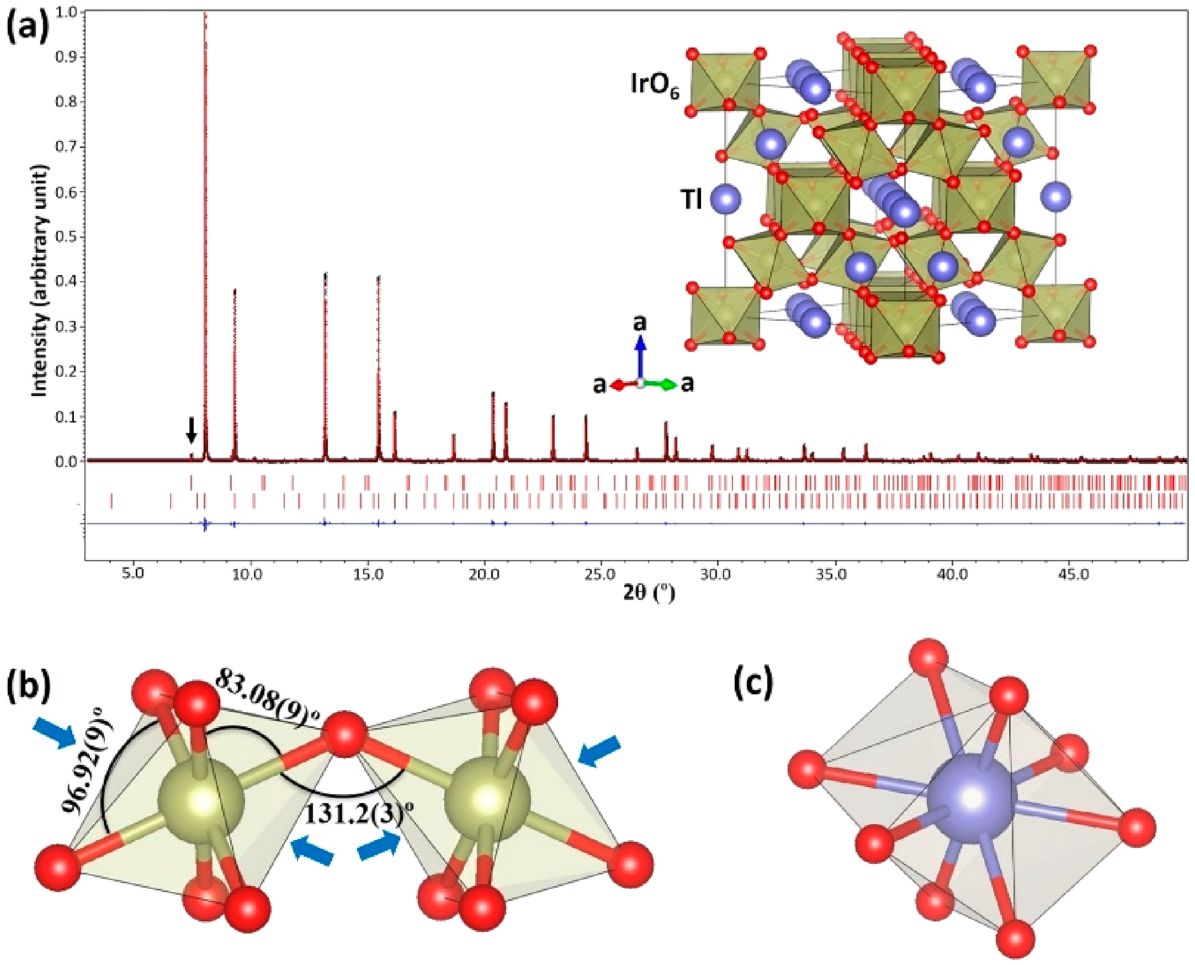

Figure 1. (a) Rietveld refined room-temperature SPXD pattern of $Tl_2Ir_2O_7$. The black asterisks are experimentally observed data. The calculated patterns are shown in red, and the blue patterns at the bottom are their difference. The lower vertical red bars indicate the diffraction positions for $Tl_2Ir_2O_7$ and the upper ones for the minor impurity IrO_2 (1.0% volume fraction). The strongest IrO_2 diffraction peak is marked with a black arrow. The crystal structure of $Tl_2Ir_2O_7$ is shown as an inset. (b) IrO_6 octahedra. The blue arrows indicate the trigonal compression of IrO_6 octahedra. (c) TlO_8 coordination in $Tl_2Ir_2O_7$.

data were carried out with the JANA2006 software,[34] and the crystal structures were drawn with the VESTA software.[35]

X-ray Absorption Near-Edge Spectroscopy (XANES). The XANES measurements were performed at the national synchrotron light source (NSLS-I and NSLS-II) at Brookhaven National Laboratory. The standard spectra were mostly collected at NSLS-I on beamlines X19A (X18B) with a Si-111 double-crystal (channel cut) monochromator. The measurement on $Tl_2Ir_2O_7$ was performed at the next-generation NSLS-II facility on the 6-BM, BMM beamline with a Si-311 double-crystal monochromator. In the data collection, both transmission mode and fluorescent measurements were made with simultaneous standards for precision energy calibration. Standard linear background and postedge normalization to unity absorption step height were used in the analysis.[36−46]

Magnetism and Electrical Resistivity. The temperature dependence of the magnetic susceptibility was measured in a VSM-7T (Quantum Design). The measurements were conducted under zero-field cooling (ZFC) and field-cooling (FC) conditions, respectively, in the temperature range of 2−300 K under an applied magnetic field of 1 and 70 kOe. Temperature-dependent electrical resistivity was measured with a direct current (dc) gauge current of 0.1 mA by the four-point method using a PPMS-14 (Quantum Design).

Density Functional Theory Plus Dynamical Mean-Field Theory (DFT+DMFT). Fully charge self-consistent DFT+DMFT calculations[47−49] implemented in Wien2k package[50] were performed with formalisms described in ref 51. The experimental crystal structure of $Tl_2Ir_2O_7$ was adopted for the calculations. In DFT calculations, the generalized gradient approximation (GGA) of Perdew−Burke−Ernzerhof (PBE) was used for the exchange-correlation functional. The muffin tin radii were chosen to be 2.28, 2.04, and 1.67 Bohr radii for Tl, Ir, and O, respectively; the size of a plane-wave basis set was determined from $R_{mt}K_{max}$ of 7.0, where R_{mt} is the smallest atomic muffin tin radius and K_{max} is the largest plane-wave vector. A 17 ×17 × 17 k-point mesh was used for the Brillouin zone integration. In DMFT calculations, the continuous-time quantum Monte Carlo method (CTQMC)[52,53] was implemented for a local impurity solver with a proper local J effective basis minimizing the sign problem. We choose a wide hybridization energy window from −10 to 10 eV with respect to the Fermi level E_F. The fully rotational invariant form was applied for a local Coulomb interaction Hamiltonian with on-site Coulomb repulsion U = 4.5 eV and J_H = 0.8 eV, where the U and J_H values were adopted in previous DFT+DMFT calculations on pyrochlore iridate compounds.[54] The maximum entropy method[55] was used for analytical continuation to obtain the self-energy on the real frequency.

RESULTS

Crystal Structure. The SPXD data of $Tl_2Ir_2O_7$ collected at room temperature (see Figure 1a) can be refined well with a cubic pyrochlore crystal structure, space group $Fd\bar{3}m$ (No. 227), which was reported for other iridium pyrochlores.[22] There was about 1.0% volume fraction of IrO_2 impurity found

https://dx.doi.org/10.1021/acs.inorgchem.0c03124
Inorg. Chem. 2021, 60, 4424−4433

Table 1. Refined Atomic Positions and Displacement Parameters of $Tl_2Ir_2O_7$ at Room Temperature[a]

atom	Wyckoff positions	occupancy	x	y	z	U_{iso} (Å^2)
Tl	16*d*	1	0.5	0.5	0.5	0.0048(2)
Ir	16*c*	1	0	0	0	0.0016(2)
O1	48*f*	1	0.3307(4)	0.125	0.125	0.0069(9)
O2	8*b*	1	0.375	0.375	0.375	0.013(3)

[a]Space group $Fd\bar{3}m$ (No. 227), a = 10.18258(5) Å, Z = 8, V = 1055.779(9) Å^3, and d = 11.392 g/cm^3. R_{wp} = 3.74%, and goodness of fit is 1.99.

in the sample. The cell parameter a = 10.18258(5) Å is comparable to that of 10.184−10.186 Å reported for $Tl_2Ru_2O_7$ synthesized at 1−3 GPa.[56] In $Tl_2Ir_2O_7$, Tl ions occupy the 16*d* ($^1/_2$, $^1/_2$, $^1/_2$) sites, Ir ions occupy the 16*c* (0, 0, 0) sites, and O anions occupy 48*f* (x, $^1/_8$, $^1/_8$) and 8b ($^3/_8$, $^3/_8$, $^3/_8$) sites. During the refinement, there was no indication of Tl/Ir antisite exchange, and there is no indication for a vacancy. We thus constrained the occupancies to 1 for all the atoms in the last refinement. The final refined atomic positions and displacement parameters are shown in Table 1. In $Tl_2Ir_2O_7$, the IrO_6 octahedra are trigonally distorted as shown in Figure 1b, and the Ir−O−Ir bond angle is 131.2°. Tl ions are coordinated with eight O forming TlO_8 polyhedra (see Figure 1c).

The bond lengths of Tl−O and Ir−O within the TlO_8 polyhedra and IrO_6 octahedra are summarized in Table 2. The

Table 2. Selected Bond Length for $Tl_2Ir_2O_7$

bond	bond length (Å)
Ir−O1	1.979(3) × 6
Tl−O1	2.492(3) × 6
Tl−O2	2.2046× 2

average Tl−O bond length, 2.420 Å, is similar to values for $Tl_2Mn_2O_7$ (2.38 Å),[57−59] for $TlNiO_3$ (2.42 Å),[60,61] for $TlCrO_3$ (2.43 Å),[62,63] for $TlMnO_3$ (2.46 Å),[64] and for $Tl_2Ru_2O_7$[56,65] (2.49 Å) with $Tl^{3+}O_8$ coordination, supporting the nominal Tl^{3+} valence state. The average Ir−O bond distances 1.979 Å, which is in reasonable agreement with those for $Y_2Ir_2O_7$[27] (1.98 Å) and for $Pr_2Ir_2O_7$[22] (2.01 Å), and $Nd_2Ir_2O_7$[13] with $Ir^{4+}O_6$ coordination. To further confirm the valence state of Ir in $Tl_2Ir_2O_7$ XANES was investigated (*vide infra*).

Ir−L_3 XANES. A comprehensive comparison of the Ir−L_3 "white line" (WL) feature of $Tl_2Ir_2O_7$ to those of the standard spectra for Sr_2CaIrO_6 (Ir^{6+}), Sr_2ScIrO_6 (Ir^{5+}), Sr_2YIrO_6 (Ir^{5+}), IrO_2 (Ir^{4+}), and La_2CuIrO_6 (Ir^{4+}) is shown in Figure 2a. An expanded and simultaneous standard-based calibrated energy scale has been used. The WL feature shows a consistent chemical shift toward lower energy from ~Ir^{6+} to ~Ir^{5+} to ~Ir^{4+} standard spectra, and the chemical shift of the $Tl_2Ir_2O_7$ spectrum is consistent with the energy for the ~Ir^{4+} standard spectrum.

For 5d oxides, the spectral structure of these WL features can also be employed as valence/configuration indicators. The WL spectral structure of octahedrally-O transition metals (TM)−L_3 involves a prominent bimodal A/B semiresolved peak. For a large class of 5d TM oxides, this structure originates from the splitting of d orbitals into lower 6-fold degenerate t_{2g} and higher 4-fold degenerate e_g multiplets due to the octahedral−O coordination.[36−46] Specifically, the bimodal A/B features are correlated to transitions into t_{2g}/e_g final hole states, respectively. The A(t_{2g}-hole-related)/B(e_g-hole-related) features are best demonstrated in a $5d^0$ Ca_2MnTaO_6 standard spectrum[38] in Figure 2b. The dramatic

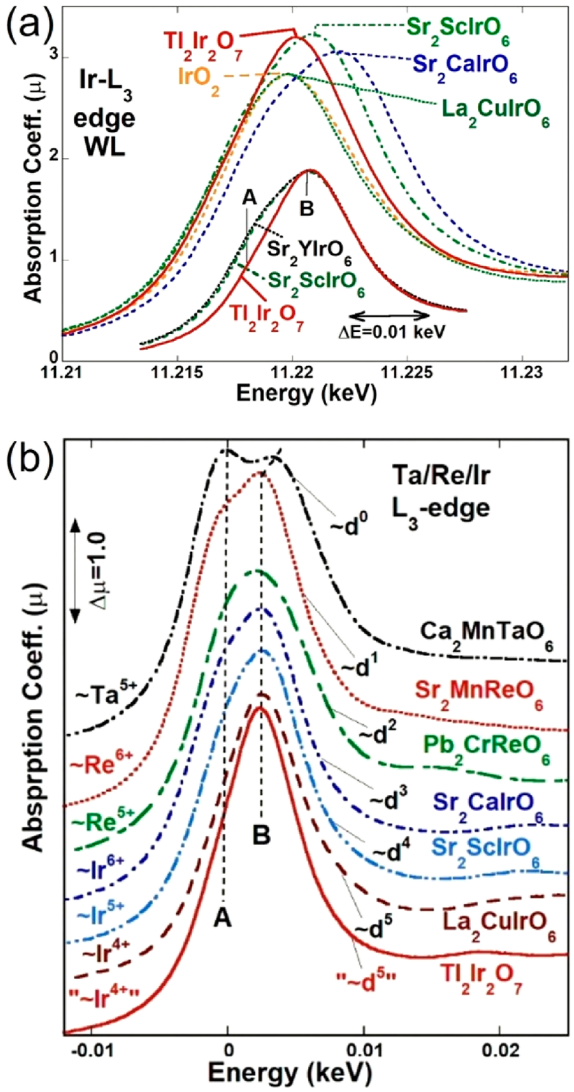

Figure 2. (a) Ir−L_3 WL feature of $Tl_2Ir_2O_7$ compared with the spectra of Sr_2CaIrO_6 (Ir^{6+}), Sr_2ScIrO_6 (Ir^{5+}), Sr_2YIrO_6 (Ir^{5+}), IrO_2 (Ir^{4+}), and La_2CuIrO_6 (Ir^{4+}). Inset shows an enlarged spectrum of $Tl_2Ir_2O_7$ superimposed with ~Ir^{5+} standard spectra to demonstrate the decrease of A-feature intensity for $Tl_2Ir_2O_7$. It should be noted that the standard spectra have been shifted to compensate for the chemical shift and rescaled for superposition. (b) Ir−L_3 WL-feature is compared with a series of standard oxides with $5d^0$ to $5d^5$ configurations. The bimodal A/B structure is correlated to transitions into t_{2g}/e_g final states, respectively; and the systematic relative loss in A-feature intensity with decreasing t_{2g} state holes.

and systematic loss of the intensity of the A-feature, with increasing t_{2g} orbital electrons, is clearly shown in Figure 2b for a series of standard spectra spanning $5d^0$−$5d^5$.[36−46] The relative A-feature intensity for the $Tl_2Ir_2O_7$ Ir−L_3 spectrum is extremely small and comparable to that of the d^5 standard

https://dx.doi.org/10.1021/acs.inorgchem.0c03124
Inorg. Chem. 2021, 60, 4424−4433

La_2CuIrO_6.[44,45] For clarification, the spectrum of $Tl_2Ir_2O_7$ is shown on an expanded scale in the inset of Figure 2a superimposed with the spectra of ~Ir^{5+} (d^4) standards, where the standard spectra were shifted to compensate for the chemical shift and rescaled for superposition. In comparison to the ~Ir^{5+} standards, the smaller A-feature intensity of the $Tl_2Ir_2O_7$ spectrum (compared to the ~Ir^{5+} standards) is demonstrated. The $Tl_2Ir_2O_7$ spectrum is sharper since it was measured on the NSLS-II beamline 6-BM, which implemented a Si-311 monochromator for higher resolution. Thus, the comparisons of the XANES spectra support a ~Ir^{4+} configuration for $Tl_2Ir_2O_7$ from the chemical shift as well as WL A/B feature perspectives.

Magnetic Properties. The temperature-dependent magnetic susceptibility curves, $\chi(T)$, are shown in Figure 3a. The

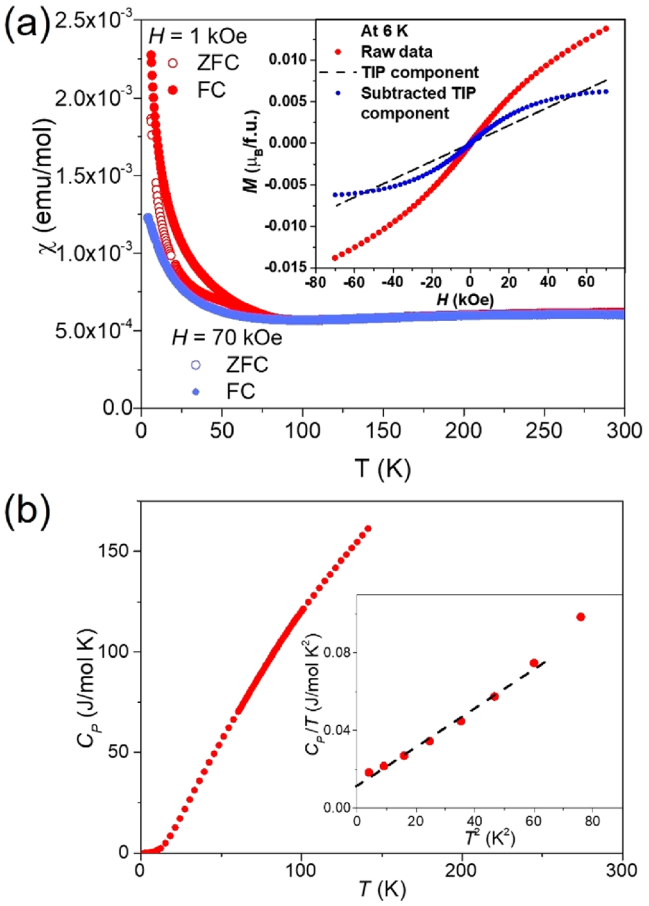

Figure 3. (a) Temperature-dependent magnetic susceptibility curves of $Tl_2Ir_2O_7$ measured at 1 and 70 kOe. The inset exhibits the field-dependent magnetization curves of $Tl_2Ir_2O_6$ measured at 6 K, and the data corrected for a temperature-independent (TIP) component. (b) Temperature-dependent specific heat curve of $Tl_2Ir_2O_7$. The inset exhibits the corresponding C_P/T vs T^2 data below 9 K.

$\chi(T)$ curves measured at 1 and 70 kOe are temperature-independent from 300−75 K, indicating a Pauli paramagnetism with a temperature-independent term $\chi_{TIP} \approx 5.7 \times 10^{-4}$ emu/mol (see the dashed lines in Figure 3a). This χ_{TIP} value is comparable to a Pauli paramagnetic value, $\chi_P \approx 5.0 \times 10^{-4}$ emu/mol, reported in other Ir pyrochlores $Pr_2Ir_2O_7$[23] and (Y, Ca)$_2Ir_2O_7$.[66] The upturn of the $\chi(T)$ curves below 75 K is possibly due to magnetic impurity. The divergence of ZFC and FC curves measured at 1 kOe was suppressed when measured at 70 kOe, which indicates that the magnetic impurity contribution can, as expected, be saturated in a magnetic field. Analysis of the 6 K field-dependent magnetization curves, $M(H)$, also supports that the upturn of the $\chi(T)$ curves is due to a small amount of ferromagnetic impurity as the magnetic impurity contribution is almost saturated at 70 kOe with a tiny magnetization value of 0.006 μ_B/f.u. as shown in the inset of Figure 3a. Specific heat was then measured from 140 to 2 K (see Figure 3b), and the specific heat curve does not show any noticeable anomaly, indicating that the upturn of the $\chi(T)$ curve is not related to magnetic order. Therefore, the low-temperature upturn of $\chi(T)$ may be related to the magnetic impurities. It should be noted that (as in the case of the Pauli paramagnetic perovskite $BaIrO_3$)[67] in the temperature range above where the Curie tail dominates that there is a perceptible minimum in $\chi(T)$ near 100 K.

Electrical Resistivity. Figure 4 shows the temperature-dependent electrical resistivity $\rho(T)$ curves. The ρ is about 2.3

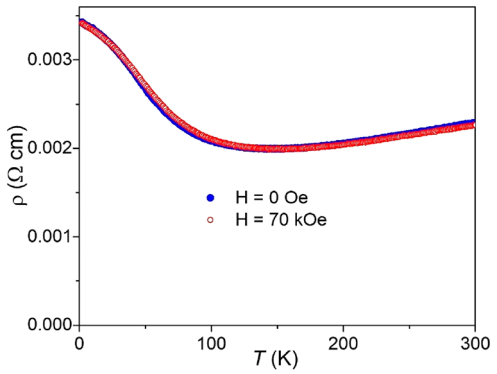

Figure 4. Temperature-dependent electrical resistivity of $Tl_2Ir_2O_7$.

mΩ cm at room temperature, which is of the same magnitude as that of $Pr_2Ir_2O_7$. $\rho(T)$ shows metallic behavior down to 150 K with the ρ decreasing with cooling, then the ρ gradually increases down to 2 K, suggesting a possible MIT. The C_p/T versus T^2 data at low temperatures (see the inset of Figure 3b) show approximately linear behavior and was fitted with the approximate Debye model $C = \gamma T + \beta T^3$, where the γ is the electronic specific heat coefficient and β is a constant related to the Debye temperature Θ_D ($\sim\beta^{-1/3}$). The fitting resulted in an estimated γ of 12(1) mJ mol^{-1} K^{-2}. The nonzero γ of 12(1) mJ mol^{-1} K^{-2}, comparable to or larger than that of 6.8−9.3 mJ mol^{-1} K^{-2} for metallic $BaIrO_3$[67] and $AOsO_3$ (A = Ca, Sr, and Ba),[68] indicates that a charge gap may not be open in $Tl_2Ir_2O_7$. Thus, the upturn of ρ at low temperatures may be related to the fact that $Tl_2Ir_2O_7$ is close to a MIT, which is further supported by the DFT+DMFT calculations showing strong electronic correlations in $Tl_2Ir_2O_7$ (*vide infra*).

DFT+DMFT Calculations. The (dimensionless) Wilson ratio, R_W, is useful to identify how strong the electronic correlation in $Tl_2Ir_2O_7$ is, and it is estimated from the measured magnetic susceptibility and electronic specific heat. From the experimental data of $\chi = 5.7 \times 10^{-4}$ emu/mol and γ = 12 mJ mol^{-1} K^{-2}, R_W = 3.6 is obtained, which is significantly away from 1 indicating the strong electron−electron interactions. Comparable R_W values have been reported for $CaCu_3Ru_4O_{12}$ (2.9)[69] and for $CeCu_6$ and $CeRu_2Si_2$ (3−4).[70] Therefore, DFT+DMFT calculations are necessary to describe the electronic structure properly. The electronic specific heat coefficient, γ, was obtained theoretically from the density of

https://dx.doi.org/10.1021/acs.inorgchem.0c03124
Inorg. Chem. 2021, 60, 4424−4433

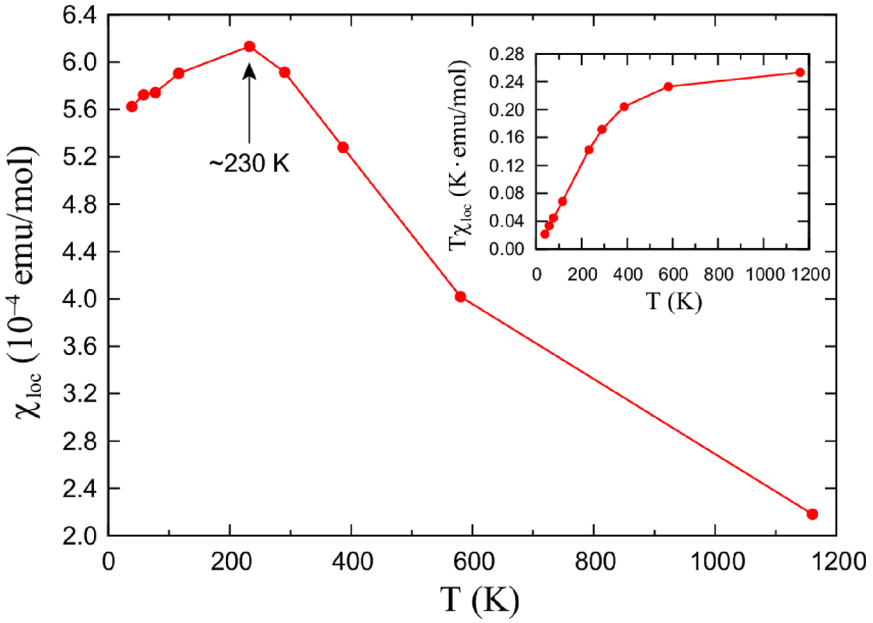

Figure 5. Temperature-dependent local magnetic susceptibility computed by DFT+DMFT. Inset shows the temperature-dependent $T\chi_{loc}$ curve. It follows the Curie−Weiss law at a very high temperature of ∼1000 K.

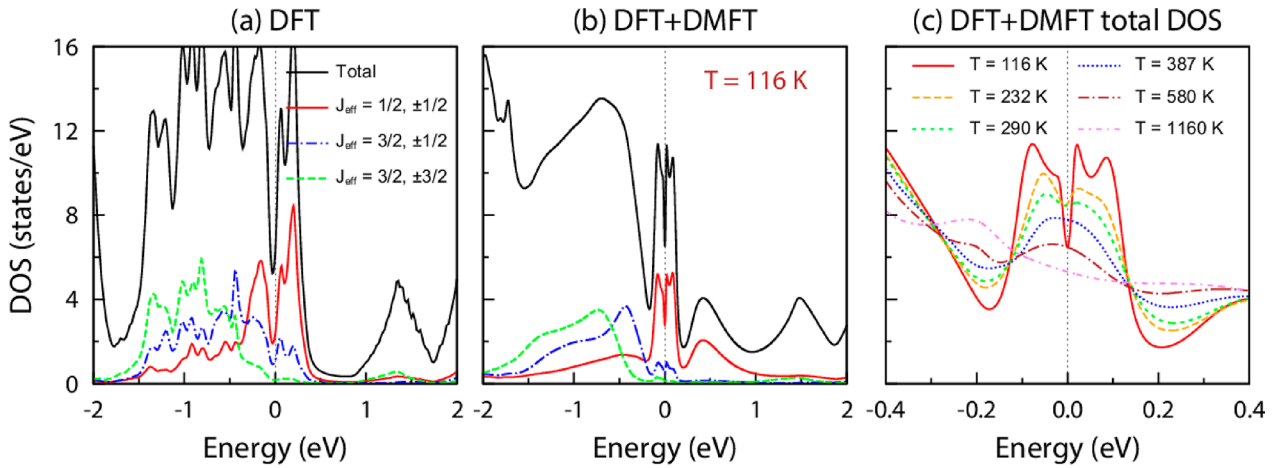

Figure 6. Density of states (DOS) of $Tl_2Ir_2O_7$ computed by (a) DFT and (b) DFT+DMFT at T = 116 K. Orbital-resolved DOS is provided in (a) and (b). (c) Temperature-dependent DOS computed by DFT+DMFT. Dip feature is realized in DFT and DFT+DMFT at low temperature.

states at the Fermi level, 6.80 and 9.99 mJ mol^{-1} K^{-2}, respectively, for DFT and DFT+DMFT (at T = 290 K). The local magnetic susceptibility, χ_{loc}, is computed in the CTQMC impurity solver by using the formula below:[71]

$$\chi_{loc} = \frac{\mu_0 (g\mu_B)^2 N_A}{k_B} \int_0^\beta d\tau \, \langle J_z(\tau) J_z(0) \rangle$$

where J_z, μ_0, g, μ_B, N_A, k_B, and β are the total angular momentum of the Ir atom, the vacuum permeability, the Landé g-factor, the Bohr magneton, the Avogadro number, the Boltzmann constant, and the inverse temperature, respectively.

Figure 5 shows the computed χ_{loc} as a function of temperature. The computed χ_{loc} at T = 230 K is χ_{loc} = 6.14 × 10^{-4} emu/mol, which is quite comparable to the experimental one at the same temperature. Therefore, DFT+DMFT produces both experimental values of γ and χ almost correctly, thereby affirming that DFT+DMFT explains well the experimental data. The computed χ_{loc} follows the Curie−Weiss law at a very high temperature (∼1000 K), which is attributed to the local magnetic moment of the Ir atom, and it is estimated to be ∼0.6 μ_B per Ir atom. It is noteworthy that the computed χ_{loc} is nearly saturated below T ∼ 230 K, where a dip feature begins to appear in the DFT+DMFT total DOS (see Figure 6c).

According to the ionic model, $Tl_2Ir_2O_7$ has Ir^{4+}, which corresponds to the d^5 electronic configuration. The Ir atoms are coordinated by six O atoms forming octahedra, as a result, the Ir 5d orbitals are split into t_{2g} and e_g orbitals; the t_{2g} orbital is further split into the effective J basis of J_{eff} = 1/2 and 3/2, because of the strong SOC.[1] From the simple ionic picture, J_{eff} = 3/2 (degeneracy: 4) is fully occupied, but J_{eff} = 1/2 (degeneracy: 2) is half-filled, thereby the Mott physics is relevant in the J_{eff} = 1/2 basis.

Figure 6a,b shows the density of states (DOS) computed by DFT and DFT+DMFT at T = 116 K, respectively, where a dip feature is realized in both DFT and DFT+DMFT calculations. Partial DOSs for J_{eff} = 1/2 and 3/2 are also provided, and their

https://dx.doi.org/10.1021/acs.inorgchem.0c03124
Inorg. Chem. 2021, 60, 4424−4433

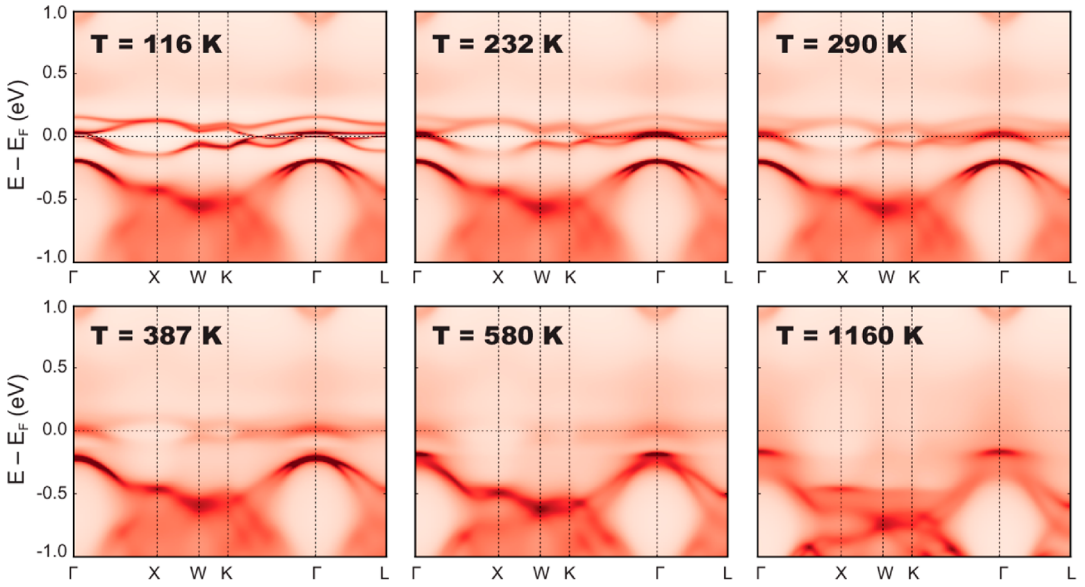

Figure 7. Temperature-dependent band dispersion of $Tl_2Ir_2O_7$ computed by DFT+DMFT.

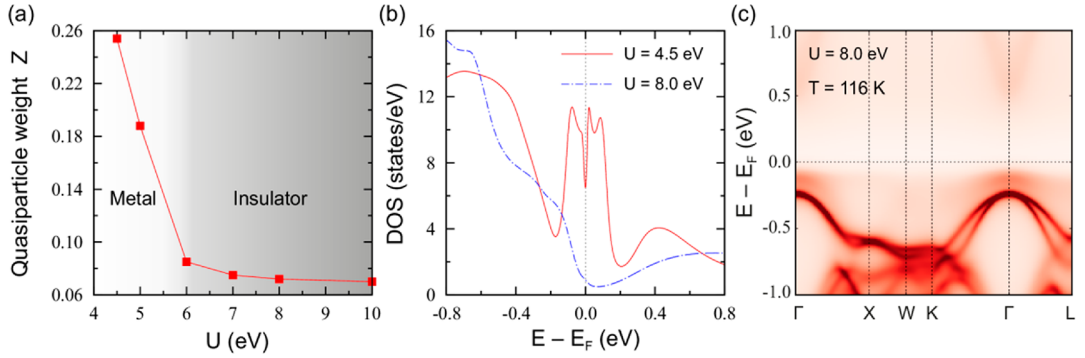

Figure 8. Electronic correlations in $Tl_2Ir_2O_7$ as a function of on-site Coulomb repulsion U (at a fixed T = 116 K) computed by DFT+DMFT. (a) Quasi-particle weight Z of J_{eff} = 1/2 as a function of U. Metal-to-insulator phase transition occurs at around U = 6 eV. (b) Density of states (DOS) calculated with different U. (c) Band dispersion at U = 8 eV. Both DOS and band dispersion clearly show an insulating phase at U = 8 eV.

occupation numbers are 1.25 (1.06) and 3.71 (2.87), respectively, in the DFT+DMFT (DFT) calculations. In the DFT+DMFT calculations, J_{eff} = 3/2 is almost fully occupied, and J_{eff} = 1/2 is nearly half-filled, whereby the Mott physics is relevant in the J_{eff} = 1/2 band. The bandwidth of J_{eff} = 1/2 is highly renormalized due to its strong correlation effect (the quasi-particle weight Z estimated from the self-energy is 0.25 at T = 116 K) as displayed in Figure 6b. It indicates that $Tl_2Ir_2O_7$ is close to a MIT driven by the Mott physics. It is supported by the DFT+DMFT studies on $Pr_2Ir_2O_7$, which has almost the same bandwidth and is at the border of a MIT.[54]

Temperature-dependent DOSs and band dispersions are displayed in Figures 6c and 7, respectively. Upon cooling, J_{eff} = 1/2 becomes coherent and has a larger spectral weight at the Fermi level. However, the dip feature is realized at low temperature, T = 116 K, and gives a small spectral weight at the Fermi level as shown in Figure 6c. The strong electronic correlations in J_{eff} = 1/2, indicate strong temperature dependence of the spectral weight near the Fermi level, which indicates that $Tl_2Ir_2O_7$ is close to a MIT and might explain the resistivity upturn at low temperatures.

The fact that $Tl_2Ir_2O_7$ is close to a MIT is further supported by Figure 8 where electronic correlations were studied as a function of on-site Coulomb repulsion U. The critical U value for a MIT is around 6 eV, and an insulating phase is realized above the critical value as shown in Figure 8. Hence, first-principles calculations clearly demonstrate that $Tl_2Ir_2O_7$ is proximal to a MIT.

DISCUSSION

Studies of iridium pyrochlores oxides, $A^{3+}{}_2Ir^{4+}{}_2O_7$ (A = lanthanide ion, Bi, and Y), indicate that the electrical properties are correlated to the ionic size of A^{3+} ions which determine the trigonal distortions of IrO_6 and Ir−O−Ir bond angles, thus affecting the hopping between neighboring Ir electrons.[9,32] $Bi_2Ir_2O_7$ and $Pr_2Ir_2O_7$ with relatively large A^{3+} cations are metallic,[10,16,19,25] while others with smaller A^{3+} ions are antiferromagnetically ordered and electrically insulating at low temperatures;[17,18,21,27,31] particularly, Nd_2Ir_2O7, $Sm_2Ir_2O_7$, and $Eu_2Ir_2O_7$ show a MIT.[12,21,28−30] The ionic radius of Tl^{3+} with TlO_8 coordination as given by Shannon is 0.98 Å which is much smaller than that of Pr^{3+} (1.126 Å) but is comparable to those of Yb^{3+} (0.985 Å) and Lu^{3+} (0.977 Å).[33] Thus, $Tl_2Ir_2O_7$ would be expected to be insulating, because both $Yb_2Ir_2O_7$ and $Lu_2Ir_2O_7$ are insulating.

In this work, the polycrystalline sample of $Tl_2Ir_2O_7$ has been successfully synthesized. The Ir^{4+} valence state is confirmed by the Ir−L_3 XANES spectrum. Magnetic susceptibility data

https://dx.doi.org/10.1021/acs.inorgchem.0c03124
Inorg. Chem. 2021, 60, 4424−4433

indicate that $Tl_2Ir_2O_7$ is Pauli paramagnetic. Temperature-dependent resistivity and the low-temperature specific heat data support the metallic state of $Tl_2Ir_2O_7$, though the resistivity shows an upturn at low temperatures. DFT +DMFT calculations also support the metallic state of $Tl_2Ir_2O_7$ and show the strong electronic correlations, which may be responsible for the resistivity upturn and indicates that $Tl_2Ir_2O_7$ is proximal to a MIT.

Both our experimental and theoretical studies show that $Tl_2Ir_2O_7$ is not an insulator, but it is a Pauli paramagnetic metal and is close to a MIT. Thus, $Tl_2Ir_2O_7$ is uniquely different from the established phase diagram of the pyrochlore iridate oxides $A^{3+}{}_2Ir^{4+}{}_2O_7$.[54] It should be noted that Takeda et al. suggested that the Tl^{3+} ionic radius of TlO_8 coordination in pyrochlore $Tl_2Ru_2O_7$ should be around 1.08−1.09 Å.[56] From the average Tl−O bond distance (2.420 Å) of $Tl_2Ir_2O_7$, a Tl^{3+} effective ionic radius of 1.02 Å with TlO_8 coordination was suggested. However, even with this increased Tl^{3+} ionic size correction, it is still not sufficient to justify the observed metallic state of $Tl_2Ir_2O_7$, as our experimental and theoretical studies indicate that $Tl_2Ir_2O_7$ is distinctive from the current $A^{3+}{}_2Ir^{4+}{}_2O_7$ phase diagram.

Figure 9 displays that the Ir−O−Ir bond angles versus the effective ionic radius of $Tl_2Ir_2O_7$ and $In_2Ir_2O_7$ do not follow

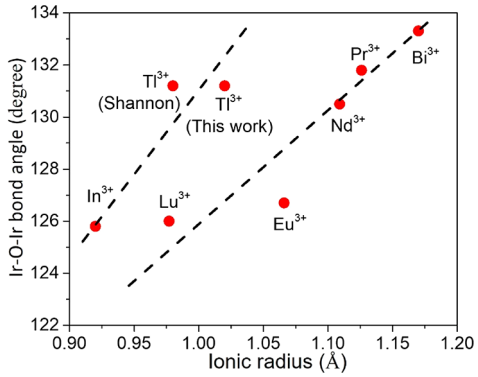

Figure 9. Ir−O−Ir bond angle of $A^{3+}{}_2Ir^{4+}{}_2O_7$ vs effective ionic radius of A^{3+}. The 8-coordinated Tl^{3+} ionic radius was taken both from Shannon,[33] and the one derived from the average Tl−O bond length of this work. The other ionic radii were taken from Shannon.[33] The dashed lines are just for the eyes.

the trend of the other rare-earth iridium pyrochlores, $A_2Ir_2O_7$, and have relatively larger Ir−O−Ir bond angles. The uniqueness of $Tl_2Ir_2O_7$ and $In_2Ir_2O_7$ may be attributed to the nature of bonding. Tl^{3+} ($4f^{14}5d^{10}6s^06p^0$) and In^{3+} ($4d^{10}5s^05p^0$) ions have fully filled f and d orbitals, whereas the trivalent rare earth ions have $4f^n5d^06s^0$ configurations (n varies from 1 for Ce^{3+} to 14 for Lu^{3+}). The fully occupied d orbitals for Tl^{3+} and In^{3+} would be far below the Fermi energy and could hinder their hybridization with the surrounding oxygens. The empty 5d orbitals of rare-earth ions would enhance their hybridization with the surrounding oxygens.

The Ir−O−Ir bond angle 131.2° of $Tl_2Ir_2O_7$ is between those of 131.8° for metallic $Pr_2Ir_2O_7$[22] and 130.50° for $Nd_2Ir_2O_7$ with MIT.[14] The Ir−O−Ir bond angle determines the overlapping of Ir−O orbitals and governs the hopping between the neighboring Ir 5d electrons and the physical properties.[9] The Ir−O−Ir bond angle of $Tl_2Ir_2O_7$ is consistent with our experimental and the DFT+DMFT calculation results that $Tl_2Ir_2O_7$ is proximal to a MIT. These findings indicate that the electronic configurations of the A^{3+} ions significantly affect the crystal structure of iridium pyrochlore oxides and the corresponding electrical and magnetic properties.

CONCLUSIONS

Pyrochlore iridate $Tl_2Ir_2O_7$ was synthesized under high-pressure conditions. $Tl_2Ir_2O_7$ crystallizes in the cubic pyrochlore crystal structure with space group $Fd\bar{3}m$ (No. 227). The Ir^{4+} oxidation state is confirmed by the Ir−L_3 XANES spectrum. The ionic size of Tl^{3+} is much smaller than that of Pr^{3+}; hence, $Tl_2Ir_2O_7$ would be expected to be insulating according to the established phase diagram of the pyrochlore iridate compounds $A^{3+}{}_2Ir^{4+}{}_2O_7$.[9] However, combined temperature-dependent magnetic susceptibility, resistivity, specific heat, and DFT+DMFT calculation data show that $Tl_2Ir_2O_7$ is a Pauli paramagnetic metal, and it is close to a MIT. This uniqueness of $Tl_2Ir_2O_7$ is attributed primarily to the electronic configuration difference of Tl^{3+} relative to the rare-earth ions, which plays a substantial role in determining the Ir−O−Ir bond angle, and the correlated electrical and magnetic properties. $Tl_2Ir_2O_7$ at the brink of localization provides a new platform to study and understand the MIT.

ASSOCIATED CONTENT

Accession Codes

CCDC 2039823 contains the supplementary crystallographic data for this paper. These data can be obtained free of charge via www.ccdc.cam.ac.uk/data_request/cif, or by emailing data_request@ccdc.cam.ac.uk, or by contacting The Cambridge Crystallographic Data Centre, 12 Union Road, Cambridge CB2 1EZ, UK; fax: +44 1223 336033.

AUTHOR INFORMATION

Corresponding Author

Martha Greenblatt − *Department of Chemistry and Chemical Biology, Rutgers, the State University of New Jersey, Piscataway, New Jersey 08854, United States;* orcid.org/0000-0002-1806-2766; Email: greenbla@chem.rutgers.edu

Authors

Hai L. Feng − *Department of Chemistry and Chemical Biology, Rutgers, the State University of New Jersey, Piscataway, New Jersey 08854, United States; Beijing National Laboratory for Condensed Matter Physics and Institute of Physics, Chinese Academy of Sciences, Beijing 100190, China;* orcid.org/0000-0002-2699-3958

Chang-Jong Kang − *Department of Physics and Astronomy, Rutgers, the State University of New Jersey, Piscataway, New Jersey 08854, United States; Department of Physics, Chungnam National University, Daejeon 34134, South Korea;* orcid.org/0000-0003-2895-4888

Zheng Deng − *Beijing National Laboratory for Condensed Matter Physics and Institute of Physics, Chinese Academy of Sciences, Beijing 100190, China*

Mark Croft − *Department of Physics and Astronomy, Rutgers, the State University of New Jersey, Piscataway, New Jersey 08854, United States*

Sizhan Liu − *Department of Physics, New Jersey Institute of Technology, Newark, New Jersey 07102, United States*

Trevor A. Tyson − *Department of Physics, New Jersey Institute of Technology, Newark, New Jersey 07102, United States;* orcid.org/0000-0001-6587-9296

https://dx.doi.org/10.1021/acs.inorgchem.0c03124
Inorg. Chem. 2021, 60, 4424−4433

Saul H. Lapidus − *Advanced Photon Source, Argonne National Laboratory, Lemont, Illinois 60439, United States;* orcid.org/0000-0002-7486-4325

Corey E. Frank − *Department of Chemistry and Chemical Biology, Rutgers, the State University of New Jersey, Piscataway, New Jersey 08854, United States*

Youguo Shi − *Beijing National Laboratory for Condensed Matter Physics and Institute of Physics, Chinese Academy of Sciences, Beijing 100190, China*

Changqing Jin − *Beijing National Laboratory for Condensed Matter Physics and Institute of Physics, Chinese Academy of Sciences, Beijing 100190, China*

David Walker − *Lamont Doherty Earth Observatory, Columbia University, Palisades, New York 10964, United States*

Gabriel Kotliar − *Department of Physics and Astronomy, Rutgers, the State University of New Jersey, Piscataway, New Jersey 08854, United States*

Complete contact information is available at: https://pubs.acs.org/10.1021/acs.inorgchem.0c03124

Notes

The authors declare no competing financial interest.

■ ACKNOWLEDGMENTS

H.L.F. thanks Prof. Jinguang Cheng for insightful discussions. C.-J.K. and G.K. were supported by the National Science Foundation grant no. DMR1733071. M.G. was supported by the Center for Computational Design of Functional Strongly Correlated Materials and Theoretical Spectroscopy under U.S. Department of Energy (DOE) grant no. DE-FOA-0001276. Use of the Advanced Photon Source at Argonne National Laboratory was supported by the DOE, Office of Science, Office of Basic Energy Sciences, under contract no. DE-AC02-06CH11357. Work at Brookhaven National Laboratory was supported by the DOE BES (DE-SC0012704) on the NSLS-II Beamlines 7BM and 6BM. Works at IOPCAS were supported by MOST (nos. 2018YFA03057001 and 2017YFB0405703) and the NSF (no. 11974407) of China through research projects. Z.D. also acknowledges the support of the Youth Innovation Promotion Association of CAS (no. 2020007).

■ REFERENCES

(1) Kim, B. J.; Jin, H.; Moon, S. J.; Kim, J. Y.; Park, B. G.; Leem, C. S.; Yu, J.; Noh, T. W.; Kim, C.; Oh, S. J.; Park, J. H.; Durairaj, V.; Cao, G.; Rotenberg, E. Novel J_{eff}= 1/2 Mott state induced by relativistic spin-orbit coupling in Sr_2IrO_4. *Phys. Rev. Lett.* **2008**, *101*, 076402.

(2) Shi, Y. G.; Guo, Y. F.; Wang, X.; Princep, A. J.; Khalyavin, D.; Manuel, P.; Michiue, Y.; Sato, A.; Tsuda, K.; Yu, S.; Arai, M.; Shirako, Y.; Akaogi, M.; Wang, N. L.; Yamaura, K.; Boothroyd, A. T. A ferroelectric-like structural transition in a metal. *Nat. Mater.* **2013**, *12*, 1024−1027.

(3) Shi, Y. G.; Guo, Y. F.; Yu, S.; Arai, M.; Belik, A. A.; Sato, A.; Yamaura, K.; Takayama-Muromachi, E.; Tian, H. F.; Yang, H. X.; et al. Continuous metal-insulator transition of the antiferromagnetic perovskite $NaOsO_3$. *Phys. Rev. B* **2009**, *80*, No. 161104(R).

(4) Yonezawa, S.; Muraoka, Y.; Matsushita, Y.; Hiroi, Z. New pyrochlore oxide superconductor $RbOs_2O_6$. *J. Phys. Soc. Jpn.* **2004**, *73*, 819−821.

(5) Feng, H. L.; Arai, M.; Matsushita, Y.; Tsujimoto, Y.; Guo, Y. F.; Sathish, C. I.; Wang, X.; Yuan, Y. H.; Tanaka, M.; Yamaura, K. High-temperature ferrimagnetism driven by lattice distortion in double perovskite Ca_2FeOsO_6. *J. Am. Chem. Soc.* **2014**, *136*, 3326−3329.

(6) Kobayashi, K. I.; Kimura, T.; Tomioka, Y.; Sawada, H.; Terakura, K.; Tokura, Y. Intergrain tunneling magnetoresistance in polycrystals of the ordered double perovskite Sr_2FeReO_6. *Phys. Rev. B: Condens. Matter Mater. Phys.* **1999**, *59*, 11159−11162.

(7) Feng, H. L.; Ghimire, M. P.; Hu, Z. W.; Liao, S. C.; Agrestini, S.; Chen, J.; Yuan, Y. H.; Matsushita, Y.; Tsujimoto, Y.; Katsuya, Y.; Tanaka, M.; Lin, H. J.; Chen, C. T.; Weng, S. C.; Valvidares, M.; Chen, K.; Baudelet, F.; Tanaka, A.; Greenblatt, M.; Tjeng, L. H.; Yamaura, K. Room-temperature ferrimagnetism of anti-site-disordered Ca_2MnOsO_6. *Phys. Rev. Mater.* **2019**, *3*, 124404.

(8) Krockenberger, Y.; Mogare, K.; Reehuis, M.; Tovar, M.; Jansen, M.; Vaitheeswaran, G.; Kanchana, V.; Bultmark, F.; Delin, A.; Wilhelm, F.; et al. Sr_2CrOsO_6: End point of a spin-polarized metal-insulator transition by 5d band filling. *Phys. Rev. B* **2007**, *75*, No. 020404(R).

(9) Witczak-Krempa, W.; Chen, G.; Kim, Y. B.; Balents, L. Correlated quantum phenomena in the strong spin-orbit regime. *Annu. Rev. Condens. Matter Phys.* **2014**, *5*, 57−82.

(10) Baker, P. J.; Möller, J. S.; Pratt, F. L.; Hayes, W.; Blundell, S. J.; Lancaster, T.; Qi, T. F.; Cao, G. Weak magnetic transitions in pyrochlore $Bi_2Ir_2O_7$. *Phys. Rev. B* **2013**, *87*, No. 180409(R).

(11) Disseler, S. M.; Dhital, C.; Amato, A.; Giblin, S. R.; de la Cruz, C.; Wilson, S. D.; Graf, M. J. Magnetic order in the pyrochlore iridates $A_2Ir_2O_7$ (A = Y, Yb). *Phys. Rev. B: Condens. Matter Mater. Phys.* **2012**, *86*, 014428.

(12) Disseler, S. M.; Dhital, C.; Hogan, T. C.; Amato, A.; Giblin, S. R.; de la Cruz, C.; Daoud-Aladine, A.; Wilson, S. D.; Graf, M. J. Magnetic order and the electronic ground state in the pyrochlore iridate $Nd_2Ir_2O_7$. *Phys. Rev. B: Condens. Matter Mater. Phys.* **2012**, *85*, 174441.

(13) Guo, H.; Ritter, C.; Komarek, A. C. Magnetic structure of Tb2Ir2O7 determined by powder neutron diffraction. *Phys. Rev. B: Condens. Matter Mater. Phys.* **2017**, *96*, 144415.

(14) Guo, H.; Ritter, C.; Komarek, A. C. Direct determination of the spin structure of Nd2Ir2O7 by means of neutron diffraction. *Phys. Rev. B: Condens. Matter Mater. Phys.* **2016**, *94*, No. 161102(R).

(15) Ishikawa, J. J.; O'Farrell, E. C. T.; Nakatsuji, S. Continuous transition between antiferromagnetic insulator and paramagnetic metal in the pyrochlore iridate $Eu_2Ir_2O_7$. *Phys. Rev. B: Condens. Matter Mater. Phys.* **2012**, *85*, 245109.

(16) Kennedy, B. J. Oxygen vacancies in pyrochlore oxides: Powder neutron diffraction study of $Pb_2Ir_2O_{6.5}$ and $Bi_2Ir_2O_{7-y}$. *J. Solid State Chem.* **1996**, *123*, 14−20.

(17) Klicpera, M.; Vlaskova, K.; Divis, M. Low-temperature properties of pyrochlore $Lu_2Ir_2O_7$. *J. Magn. Magn. Mater.* **2020**, *506*, 166793.

(18) Krajewska, A.; Takayama, T.; Dinnebier, R.; Yaresko, A.; Ishii, K.; Isobe, M.; Takagi, H. Almost pure J_{eff} = 1/2 Mott state of $In_2Ir_2O_7$ in the limit of reduced intersite hopping. *Phys. Rev. B* **2020**, *101*, No. 121101(R).

(19) Machida, Y.; Nakatsuji, S.; Maeno, Y.; Tayama, T.; Sakakibara, T. Geometrical frustration and spin-liquid behavior of the metallic pyrochlore antiferromagnet $Pr_2Ir_2O_7$. *J. Magn. Magn. Mater.* **2007**, *310*, 1328−1330.

(20) Machida, Y.; Nakatsuji, S.; Maeno, Y.; Tayama, T.; Sakakibara, T.; Onoda, S. Unconventional anomalous Hall effect enhanced by a noncoplanar spin texture in the frustrated Kondo lattice $Pr_2Ir_2O_7$. *Phys. Rev. Lett.* **2007**, *98*, 057203.

(21) Matsuhira, K.; Wakeshima, M.; Nakanishi, R.; Yamada, T.; Nakamura, A.; Kawano, W.; Takagi, S.; Hinatsu, Y. Metal-insulator transition in pyrochlore iridates $Ln_2Ir_2O_7$ (Ln = Nd, Sm, and Eu). *J. Phys. Soc. Jpn.* **2007**, *76*, 043706.

(22) Millican, J. N.; Macaluso, R. T.; Nakatsuji, S.; Machida, Y.; Maeno, Y.; Chan, J. Y. Crystal growth and structure of $R_2Ir_2O_7$ (R = Pr, Eu) using molten KF. *Mater. Res. Bull.* **2007**, *42*, 928−934.

(23) Nakatsuji, S.; Machida, Y.; Maeno, Y.; Tayama, T.; Sakakibara, T.; van Duijn, J.; Balicas, L.; Millican, J. N.; Macaluso, R. T.; Chan, J. Y. Metallic spin-liquid behavior of the geometrically frustrated Kondo lattice $Pr_2Ir_2O_7$. *Phys. Rev. Lett.* **2006**, *96*, 087204.

(24) Nakayama, M.; Kondo, T.; Tian, Z.; Ishikawa, J. J.; Halim, M.; Bareille, C.; Malaeb, W.; Kuroda, K.; Tomita, T.; Ideta, S.; Tanaka, K.; Matsunami, M.; Kimura, S.; Inami, N.; Ono, K.; Kumigashira, H.; Balents, L.; Nakatsuji, S.; Shin, S. Slater to Mott crossover in the metal to insulator transition of $Nd_2Ir_2O_7$. *Phys. Rev. Lett.* **2016**, *117*, 056403.
(25) Qi, T. F.; Korneta, O. B.; Wan, X. G.; DeLong, L. E.; Schlottmann, P.; Cao, G. Strong magnetic instability in correlated metallic Bi_2Ir_2O. *J. Phys.: Condens. Mater.* **2012**, *24*, 345601.
(26) Sakata, M.; Kagayama, T.; Shimizu, K.; Matsuhira, K.; Takagi, S.; Wakeshima, M.; Hinatsu, Y. Suppression of metal-insulator transition at high pressure and pressure-induced magnetic ordering in pyrochlore oxide $Nd_2Ir_2O_7$. *Phys. Rev. B* **2011**, *83*, No. 041102(R).
(27) Shapiro, M. C.; Riggs, S. C.; Stone, M. B.; de la Cruz, C. R.; Chi, S.; Podlesnyak, A. A.; Fisher, I. R. Structure and magnetic properties of the pyrochlore iridate $Y_2Ir_2O_7$. *Phys. Rev. B: Condens. Matter Mater. Phys.* **2012**, *85*, 214434.
(28) Taira, N.; Wakeshima, M.; Hinatsu, Y. Magnetic properties of iridium pyrochlores $R_2Ir_2O_7$ (R = Y, Sm, Eu and Lu). *J. Phys.: Condens. Matter* **2001**, *13*, 5527−5533.
(29) Tomiyasu, K.; Matsuhira, K.; Iwasa, K.; Watahiki, M.; Takagi, S.; Wakeshima, M.; Hinatsu, Y.; Yokoyama, M.; Ohoyama, K.; Yamada, K. Emergence of magnetic long-range order in frustrated pyrochlore $Nd_2Ir_2O_7$ with metal-insulator transition. *J. Phys. Soc. Jpn.* **2012**, *81*, 034709.
(30) Ueda, K.; Fujioka, J.; Yang, B. J.; Shiogai, J.; Tsukazaki, A.; Nakamura, S.; Awaji, S.; Nagaosa, N.; Tokura, Y. Magnetic field-induced insulator-semimetal transition in a Pyrochlore $Nd_2Ir_2O_7$. *Phys. Rev. Lett.* **2015**, *115*, 056402.
(31) Yanagishima, D.; Maeno, Y. Metal-nonmetal changeover in pyrochlore iridates. *J. Phys. Soc. Jpn.* **2001**, *70*, 2880−2883.
(32) Ishii, F.; Mizuta, Y. P.; Kato, T.; Ozaki, T.; Weng, H. M.; Onoda, S. First-principles study on cubic pyrochlore iridates $Y_2Ir_2O_7$ and $Pr_2Ir_2O_7$. *J. Phys. Soc. Jpn.* **2015**, *84*, 073703.
(33) Shannon, R. D. Revised effective ionic-radii and systematic studies of interatomic distances in halides and chalcogenides. *Acta Crystallogr., Sect. A: Cryst. Phys., Diffr., Theor. Gen. Crystallogr.* **1976**, *32*, 751−767.
(34) Petříček, V.; Dušek, M.; Palatinus, L. Crystallographic computing system JANA2006: General features. *Z. Kristallogr.-Cryst. Mater.* **2014**, *229*, 345−352.
(35) Momma, K.; Izumi, F. VESTA 3 for three-dimensional visualization of crystal, volumetric and morphology data. *J. Appl. Crystallogr.* **2011**, *44*, 1272−1276.
(36) Popov, G.; Greenblatt, M.; Croft, M. Large effects of A-site average cation size on the properties of the double perovskites $Ba_{2-x}Sr_xMnReO_6$: A d^5-d^1 system. *Phys. Rev. B: Condens. Matter Mater. Phys.* **2003**, *67*, 024406.
(37) Lin, Q. S.; Greenblatt, M.; Croft, M. Evolution of structure and magnetic properties in electron-doped double perovskites, $Sr_{2-x}La_xMnWO_6$ (0×1). *J. Solid State Chem.* **2005**, *178*, 1356−1366.
(38) Mandal, T. K.; Poltavets, V. V.; Croft, M.; Greenblatt, M. Synthesis, structure and magnetic properties of $A_2MnB'O_6$ (A = Ca, Sr; B′ = Sb, Ta) double perovskites. *J. Solid State Chem.* **2008**, *181*, 2325−2331.
(39) Retuerto, M.; Li, M. R.; Go, Y. B.; Ignatov, A.; Croft, M.; Ramanujachary, K. V.; Herber, R. H.; Nowik, I.; Hodges, J. P.; Dachraoui, W.; Hadermann, J.; Greenblatt, M. High magnetic ordering temperature in the perovskites $Sr_{4-x}La_xFe_3ReO_{12}$ (x = 0.0, 1.0, 2.0). *J. Solid State Chem.* **2012**, *194*, 48−58.
(40) Li, M. R.; Walker, D.; Retuerto, M.; Sarkar, T.; Hadermann, J.; Stephens, P. W.; Croft, M.; Ignatov, A.; Grams, C. P.; Hemberger, J.; Nowik, I.; Halasyamani, P. S.; Tran, T. T.; Mukherjee, S.; Dasgupta, T. S.; Greenblatt, M. Polar and magnetic Mn_2FeMO_6 (M = Nb, Ta) with $LiNbO_3$-type structure: high-pressure synthesis. *Angew. Chem., Int. Ed.* **2013**, *52*, 8406−8410.
(41) Kayser, P.; Martinez-Lope, M. J.; Alonso, J. A.; Retuerto, M.; Croft, M.; Ignatov, A.; Fernandez-Diaz, M. T. Crystal structure, phase transitions, and magnetic properties of iridium perovskites Sr_2MIrO_6 (M = Ni, Zn). *Inorg. Chem.* **2013**, *52*, 11013−11022.
(42) Kayser, P.; Martinez-Lope, M. J.; Alonso, J. A.; Retuerto, M.; Croft, M.; Ignatov, A.; Fernandez-Diaz, M. T. Crystal and magnetic structure of Sr_2MIrO_6 (M = Ca, Mg) double perovskites - a neutron diffraction study. *Eur. J. Inorg. Chem.* **2014**, *2014*, 178−185.
(43) Kayser, P.; Alonso, J. A.; Mompean, F. J.; Retuerto, M.; Croft, M.; Ignatov, A.; Fernandez-Diaz, M. T. Crystal and magnetic structure of Sr_2BIrO_6 (B = Sc, Ti, Fe, Co, In) in the framework of multivalent iridium double perovskites. *Eur. J. Inorg. Chem.* **2015**, *2015*, 5027−5038.
(44) Li, M. R.; Retuerto, M.; Deng, Z.; Sarkar, T.; Sanchez-Benitez, J.; Croft, M. C.; Dasgupta, T. S.; Das, T.; Tyson, T. A.; Walker, D.; Greenblatt, M. Strong electron hybridization and fermi-to-non-fermi liquid transition in $LaCu_3Ir_4O_{12}$. *Chem. Mater.* **2015**, *27*, 211−217.
(45) Feng, H. L.; Deng, Z.; Wu, M. X.; Croft, M.; Lapidus, S. H.; Liu, S. Z.; Tyson, T. A.; Ravel, B. D.; Quackenbush, N. F.; Frank, C. E.; Jin, C. Q.; Li, M. R.; Walker, D.; Greenblatt, M. High-pressure synthesis of Lu_2NiIrO_6 with ferrimagnetism and large coercivity. *Inorg. Chem.* **2019**, *58*, 397−404.
(46) Frank, C. E.; McCabe, E. E.; Orlandi, F.; Manuel, P.; Tan, X. Y.; Deng, Z.; Croft, M.; Cascos, V.; Emge, T.; Feng, H. L.; Lapidus, S.; Jin, C. Q.; Wu, M. X.; Li, M. R.; Ehrlich, S.; Khalid, S.; Quackenbush, N.; Yu, S.; Walker, D.; Greenblatt, M. Mn_2CoReO_6: a robust multisublattice antiferromagnetic perovskite with small A-site cations. *Chem. Commun.* **2019**, *55*, 3331−3334.
(47) Georges, A.; Kotliar, G.; Krauth, W.; Rozenberg, M. J. Dynamical mean-field theory of strongly correlated fermion systems and the limit of infinite dimensions. *Rev. Mod. Phys.* **1996**, *68*, 13.
(48) Kotliar, G.; Savrasov, S. Y.; Haule, K.; Oudovenko, V. S.; Parcollet, O.; Marianetti, C. A. Electronic structure calculations with dynamical mean-field theory. *Rev. Mod. Phys.* **2006**, *78*, 865.
(49) Held, K. Electronic structure calculations using dynamical mean field theory. *Adv. Phys.* **2007**, *56*, 829.
(50) Blaha, P.; Schwarz, K.; Tran, F.; Laskowski, R.; Madsen, G. K. H.; Marks, L. D. WIEN2k: An APW+lo program for calculating the properties of soldis. *J. Chem. Phys.* **2020**, *152*, 074101.
(51) Haule, K.; Yee, C.-H.; Kim, K. Dynamical mean-field theory within the full-potential methods: Electronic structure of CeIrIn5, CeCoIn5, and CeRhIn5. *Phys. Rev. B: Condens. Matter Mater. Phys.* **2010**, *81*, 195107.
(52) Werner, P.; Comanac, A.; de' Medici, L.; Troyer, M.; Millis, A. J. Continuous-time solver for quantum impurity models. *Phys. Rev. Lett.* **2006**, *97*, 076405.
(53) Haule, K. Quantum Monte Carlo impurity solver for cluster dynamical mean-field theory and electronic structure calculations with adjustable cluster base. *Phys. Rev. B: Condens. Matter Mater. Phys.* **2007**, *75*, 155113.
(54) Zhang, H.; Haule, K.; Vanderbilt, D. Metal-insulator transition and topological properties of pyrochlore iridates. *Phys. Rev. Lett.* **2017**, *118*, 026404.
(55) Jarrell, M.; Gubernatis, J. E. Bayesian inference and the analytic continuation of imaginary-time quantum Monte Carlo data. *Phys. Rep.* **1996**, *269*, 133.
(56) Takeda, T.; Nagata, M.; Kobayashi, H.; Kanno, R.; Kawamoto, Y.; Takano, M.; Kamiyama, T.; Izumi, F.; Sleight, A.W. High-pressure synthesis, crystal structure, and metal-semiconductor transitions in the $Tl_2Ru_2O_{7-delta}$ pyrochlore. *J. Solid State Chem.* **1998**, *140*, 182−193.
(57) Shimakawa, Y.; Kubo, Y. Crystal structure, magnetic and transport properties, and electronic and structure of colossal magnetoresistance $Tl_2Mn_2O_7$ pyrochlore. *Mater. Sci. Eng., B* **1999**, *63*, 44−48.
(58) Shimakawa, Y.; Kubo, Y.; Manako, T. Giant magnetoresistance in $Tl_2Mn_2O_7$ with the pyrochlore structure. *Nature* **1996**, *379*, 53−55.
(59) Subramanian, M. A.; Toby, B. H.; Ramirez, A. P.; Marshall, W. J.; Sleight, A. W.; Kwei, G. H. Colossal magnetoresistance without Mn^{3+}/Mn^{4+} double exchange in the stoichiometric pyrochlore $Tl_2Mn_2O_7$. *Science* **1996**, *273*, 81−84.
(60) Kim, S. J.; Demazeau, G.; Alonso, J. A.; Choy, J. H. High pressure synthesis and crystal structure of a new Ni(III) perovskite: $TlNiO_3$. *J. Mater. Chem.* **2001**, *11*, 487−492.

https://dx.doi.org/10.1021/acs.inorgchem.0c03124
Inorg. Chem. 2021, 60, 4424−4433

(61) Kim, S. J.; Martinez-Lope, M. J.; Fernandez-Diaz, M. T.; Alonso, J. A.; Presniakov, I.; Demazeau, G. Evidence of Ni(III) disproportionation in the $TlNiO_3$ perovskite lattice through neutron powder diffraction and Mossbauer spectroscopy. *Chem. Mater.* **2002**, *14*, 4926−4932.
(62) Yi, W.; Matsushita, Y.; Katsuya, Y.; Yamaura, K.; Tsujimoto, Y.; Presniakov, I. A.; Sobolev, A. V.; Glazkova, Y. S.; Lekina, Y. O.; Tsujii, N.; Nimori, S.; Takehana, K.; Imanaka, Y.; Belik, A. A. High-pressure synthesis, crystal structure and magnetic properties of $TlCrO_3$ perovskite. *Dalton Trans.* **2015**, *44*, 10785−10794.
(63) Ding, L.; Manuel, P.; Khalyavin, D. D.; Orlandi, F.; Kumagai, Y.; Oba, F.; Yi, W.; Belik, A. A. Unusual magnetic structure of the high-pressure synthesized perovskites $ACrO_3$ (A = Sc, In, Tl). *Phys. Rev. B: Condens. Matter Mater. Phys.* **2017**, *95*, 054432.
(64) Yi, W.; Kumagai, Y.; Spaldin, N. A.; Matsushita, Y.; Sato, A.; Presniakov, I. A.; Sobolev, A. V.; Glazkova, Y. S.; Belik, A. A. Perovskite-structure $TlMnO_3$: A new Manganite with new properties. *Inorg. Chem.* **2014**, *53*, 9800−9808.
(65) Mori, D.; Sonoyama, N.; Yamada, A.; Kanno, R.; Azuma, M.; Takano, M.; Suda, K.; Ishizawa, N. Single-crystal growth of $Tl_2Ru_2O_7$ pyrochlore using high-pressure and flux method. *J. Solid State Chem.* **2006**, *179*, 935−940.
(66) Fukazawa, H.; Maeno, Y. Filling control of the pyrochlore oxide $Y_2Ir_2O_7$. *J. Phys. Soc. Jpn.* **2002**, *71*, 2578−2579.
(67) Cheng, J. G.; Ishii, T.; Kojitani, H.; Matsubayashi, K.; Matsuo, A.; Li, X.; Shirako, Y.; Zhou, J. S.; Goodenough, J. B.; Jin, C. Q.; Akaogi, M.; Uwatoko, Y. High-pressure synthesis of the $BaIrO_3$ perovskite: A Pauli paramagnetic metal with a Fermi liquid ground state. *Phys. Rev. B: Condens. Matter Mater. Phys.* **2013**, *88*, 205114.
(68) Shi, Y. G.; Guo, Y. F.; Shirako, Y. C.; Yi, W.; Wang, X.; Belik, A. A.; Matsushita, Y.; Feng, H. L.; Tsujimoto, Y.; Arai, M.; Wang, N. L.; Akaogi, M.; Yamaura, K. High-pressure synthesis of 5d cubic perovskite $BaOsO_3$ at 17 GPa: Ferromagnetic evolution over 3d to 5d Series. *J. Am. Chem. Soc.* **2013**, *135*, 16507−16516.
(69) Kao, T.-H.; Sakurai, H.; Yu, S.; Kato, H.; Tsujii, N.; Yang, H.-D. Oeigin of the magnetic susceptibility maximum in $CaCu_3Ru_4O_{12}$ and electronic states in the A-site substituted compounds. *Phys. Rev. B: Condens. Matter Mater. Phys.* **2017**, *96*, 024402.
(70) Krug von Nidda, H.-A.; Bulla, R.; Buttgen, N.; Heinrich, M.; Loidl, A. Heavy fermions in transition metals and transition-metal oxides. *Eur. Phys. J. B* **2003**, *34*, 399−407.
(71) Haule, K.; Kotliar, G. Coherence-incoherence crossover in the normal state of iron-oxypnictides and importance of the Hund's rule coupling. *New J. Phys.* **2009**, *11*, 025021.

https://dx.doi.org/10.1021/acs.inorgchem.0c03124
Inorg. Chem. 2021, 60, 4424−4433